Available online at www.sciencedirect.com
ScienceDirect
Comput. Methods Appl. Mech. Engrg. 285 (2015) 166–187
Computer methods in applied mechanics and engineering
www.elsevier.com/locate/cma

Topology optimization of viscoelastic structures using a time-dependent adjoint method

Kai A. James*, Haim Waisman

Columbia University, Department of Civil Engineering and Engineering Mechanics, New York, NY, United States

Received 4 June 2014; received in revised form 20 October 2014; accepted 10 November 2014
Available online 18 November 2014

Highlights

- Topology optimization of structures accounting for viscoelastic creep response is proposed.
- The algorithm uses a time dependent viscoelastic finite element analysis method.
- Design constraints are based on the full viscoelastic response of the structures.
- A time-dependent adjoint formula is used for computing sensitivities.
- The optimized designs are lighter than those obtained through linear elastic analysis.

Abstract

We present a mathematical framework for producing optimal designs of structures that exhibit viscoelastic creep deformation. Using a linear viscoelastic finite element model, we implement a corresponding time-dependent adjoint sensitivity formulation. The resulting formula is then incorporated into a computational topology optimization framework in order to achieve optimal topologies based on the expected lifespan or operating cycle of the structure. Designs are optimized for minimum mass subject to a constraint on the maximum local deflection. We validate the method using several two-dimensional numerical examples that include design-dependent gravitational loading (self-weight) and time-dependent applied loads. Creep plots are used to quantify the impact of the viscoelastic optimization method. The results show that the design of the optimal structure is highly dependent on the load duration and the complete load history. This result supports the design premise that it is necessary to account for the full viscoelastic response of the structure when designing for optimal long-term performance.

Keywords: Topology optimization; Viscoelasticity; Creep; Adjoint sensitivity analysis

1. Introduction

Since its introduction in the late 80s [1,2], topology optimization has grown into a pervasive and versatile tool for designing structures for a wide variety of applications. However despite this growth, the bulk of topology optimization

* Corresponding author. Tel.: +1 917 868 5546; fax: +1 212 854 6267.
E-mail address: kai.james@columbia.edu (K.A. James).

http://dx.doi.org/10.1016/j.cma.2014.11.012
0045-7825/

research remains focused on elastic materials, with only a handful of studies investigating problems involving inelasticity. This represents a significant void within the literature as purely elastic models are unreliable for large classes of engineering structures and materials. Creep deformation is one such area, which is of growing interest within the structural mechanics community but which has remained largely absent from the structural optimization literature. *Creep* is a viscoelastic phenomenon that is characterized by time-dependent deformation of a structure subject to constant applied loading, particularly when exposed to high temperatures. Design for mitigating creep deformation is an especially salient problem for aging structures and engineering systems operating in high-temperature environments such as jet engines and computer components [3].

While the focus on elastic problems continues to dominate the literature, there have been some notable exceptions, particularly in the areas of plasticity and damage. One of the earliest papers to explore the use of inelastic material models in combination with topology optimization was a 1996 paper by Mayer et al. [4]. Here the authors used an elastoplastic model to simulate the deformation of an automobile's rear rail, when subject to impact loading. The resulting nonlinear analysis was incorporated into a topology optimization framework for crashworthiness in the optimized designs. Since then, a number of authors have also applied plasticity-based topology optimization to the problem of design for crashworthiness [5–8]. Shortly after Mayer et al. [4] published their seminal work on elastoplastic topology optimization for crashworthiness, Swan and Kosaka [9] published a similarly pioneering study on topology optimization of inelastic structures, which included a formulation for viscoelasticity in addition to elastoplastic design. A year later, in 1998, Maute et al. [10] published a third paper on elastoplastic topology optimization in which they used a model based on the von Mises yield criterion in order to optimize structures for maximum ductility.

More recently, several authors have begun to investigate the use of nonlinear continuum damage models [11] in optimal topology design. In a 2008 paper, Desmorat and Desmorat [12] used a damage-based approach to model plasticity due to cyclical loading. They then used topology optimization to reduce fatigue and maximize the lifespan of the structure. Further examples can be found in a series of papers by Amir [13] and Amir and Sigmund [14] in which they used a brittle damage model to simulate damage accumulation and softening in concrete. Here topology optimization was used to optimize the layout of both the concrete matrix, as well as a series of steel reinforcements. Both papers used a path-dependent adjoint formulation in order to efficiently compute the design sensitivities. In a subsequent paper, the current authors used a similar brittle damage formulation to perform topology optimization of damage-resistant structures by implementing a global damage constraint [15]. In that study, we implemented a coupled, path-dependent adjoint sensitivity method, whereas in the current study, we use a time-dependent viscoelastic adjoint sensitivity method. By contrast, Swan and Kosaka [9] used a direct sensitivity analysis method in their viscoelastic topology optimization framework. In general, the direct approach is more computationally expensive for topology optimization problems since the design space tends to be relatively large. Since the publication of that paper in 1997, viscoelastic topology design has been investigated only sporadically, and most often in the context of viscoelastic damping. Various authors have used viscoelastic topology optimization to obtain optimal structural behavior in response to dynamic loading [16–20]. Additionally, a 2012 study by Jensen et al. [21] investigated the use of topology optimization for the design of viscoelastic rectifiers comprised of oscillating valves, whose actuation was due to the inertial properties of the fluid being regulated. Still, few in the design optimization community have addressed the problem of creep deformation due to sustained loading, and its impact on the longterm performance of structures, which is an important aspect of aging structures.

The current study addresses this problem by incorporating creep considerations into a topology optimization algorithm using a time-dependent, nonlinear viscoelastic finite element model. We then derive a corresponding original time-dependent adjoint sensitivity formulation, which is used to rapidly and accurately compute the design sensitivities. The method is demonstrated on several example problems using a variety of loading scenarios including gravitational and time-dependent loading. The remaining sections of the article are laid out as follows: Section 2 contains an overview of the design optimization problem along with a brief description of the SIMP method [22,2], which is used to parameterize the structural design. Section 3 outlines the theory and methodology behind the modeling of viscoelastic materials, and provides a derivation of the viscoelastic finite element formulation used to discretize and solve the analysis problem. In Section 4 we derive the adjoint sensitivity analysis method and summarize the algorithm used to implement the procedure computationally. Section 5 describes the example problems and presents the results along with some discussion and analysis. Finally, in Section 6 we conclude the paper with a summary highlighting the most significant contributions.

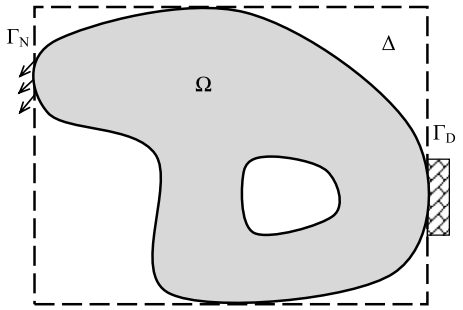

Fig. 1. The generalized material distribution problem, with surface traction (Γ_N) and fixed (Γ_D) boundary conditions.

2. Topology optimization

2.1. Problem overview

In the current framework, the structural design task is approached as a material distribution problem. We begin by defining a *working domain*, i.e. a physical region in which material must be systematically distributed in order to achieve optimal structural performance. The general problem is illustrated in Fig. 1. In the figure, the working domain is represented by Δ, while the material domain is given by Ω. In mathematical terms, Δ is a bounded domain in d-dimensional space ($\mathbb{R}^d$, with $d \in \{2, 3\}$), which contains all admissible shapes Ω. The symbols Γ_N and Γ_D represent surfaces on which traction (Neumann) and fixed (Dirichlet) boundary conditions are applied respectively.

During the optimization process, one seeks an optimal material distribution Ω^*, which minimizes some cost function, f_o, while satisfying specified design constraints, c. The cost function and the constraint functions are generally dependent on the structural state variables, which, in this case, are given by the displacement field, $\mathbf{u}$, and may also have some direct dependence on Ω. Therefore, the generalized optimization problem can be written mathematically as follows.

$$\begin{aligned} &\min_{\Omega \subset \Delta} \; f_o(\Omega) \\ &\text{subject to} : c_i(\Omega) \geq 0, \quad i = 1, 2, \ldots, n_i \\ &\qquad\qquad \tilde{c}_j(\Omega) = 0, \quad j = 1, 2, \ldots, n_e. \end{aligned} \tag{1}$$

Here $\{\tilde{c}_i\}$ and $\{c_j\}$ denote the sets of equality and inequality constraints, while n_i and n_e, represent the number of each type of constraint. In the current study, we minimize the structural mass so that $f_o = \int_\Omega \mathrm{d}V$, where V represents volume. In the examples presented, the constraint functions are chosen as the viscoelastic deformation, which must remain below a given threshold At each point in the optimization search, the structural governing equations are used to obtain the displacement state of the structure, and the resulting information is used to guide the search. We derive these equations by satisfying equilibrium equations and boundary conditions, which are given by

$$\nabla \cdot \boldsymbol{\sigma} + \mathbf{b} = 0 \quad \text{in } \Omega \tag{2}$$

$$\boldsymbol{\sigma} \cdot \mathbf{n} = \boldsymbol{\tau} \quad \text{on } \Gamma_N \tag{3}$$

$$\mathbf{u} = \mathbf{0} \quad \text{on } \Gamma_D \tag{4}$$

where $\boldsymbol{\sigma}$ is the stress tensor, $\nabla\cdot$ is the divergence operator, $\mathbf{b}$ represents all body forces acting on Ω, and $\boldsymbol{\tau}$ denotes surface tractions. The symbol $\mathbf{n}$ denotes the unit vector normal to the material surface. These equations are combined with the kinematic relation for small displacements, $\boldsymbol{\varepsilon} = \boldsymbol{\nabla}_s \mathbf{u}$, where $\nabla_s = \frac{1}{2}(\nabla^{\mathrm{T}} + \nabla)$, and the constitutive relation (discussed in Section 3.3) to comprise the strong form of the governing equations for the structure.

2.2. Design parameterization

The process of solving for the state of the structure based on a given design Ω, is hereafter referred to as the *forward* problem, as this is the primary task in structural mechanics. By contrast, the process of solving for the optimal design (or design *step*) for a specified performance objective and based on the current structural state, is referred to as

the *inverse* problem. The combined design optimization problem is discretized using finite element analysis combined with the SIMP (*solid isotropic material penalization*) method [22,2] method for determining the optimal distribution of material. In accordance with the SIMP formulation, within each element the effective material properties are evaluated based on the following equation.

$$\mathcal{E}^*_{\text{eff}} = \rho^p \mathcal{E}^*_0. \tag{5}$$

Here, $\mathcal{E}^*$ represents a generic constitutive operator, ρ is the relative material density, which ranges from 0 to 1. The set of all relative material densities for each element, $\boldsymbol{\rho}$. is treated as the independent variable in the optimization problem, as this vector fully describes the distribution of material within the structure. The SIMP penalization constant, p, is chosen as some number greater than 1, to ensure that intermediate densities are penalized and removed from the optimal design. Note that the subscript "eff" indicates the effective value corresponding to the penalized material, while the subscript "0" indicates a value corresponding to the unpenalized bulk material. To avoid the mesh-dependency and other numerical instabilities encountered with element-based topology optimization methods [23,24], we implement the density filtering technique proposed by Bruns and Tortorelli [25].

3. Viscoelasticity and creep deformation

Creep deformation can be observed in many engineering structures when they are made to withstand longterm, sustained loading. Although creep is often considered to be a high-temperature phenomenon, this interpretation is imprecise since creep is actually dependent on the ratio of the operating temperature to the melting temperature (in Kelvin) [26]. It is also true that in the context of solid mechanics, creep is often associated with fracture. Indeed, historically many scientists and engineers have focused their efforts on ascertaining the time to fracture [27–29]. However, more recently in various applications such as turbine blades, critical deflection has been adopted as the most salient failure criterion [26]. In this section we discuss the theoretical framework used to model creep deflection, and describe the numerical implementation of the corresponding viscoelastic finite element method used to perform the analysis.

3.1. Rheological modeling

When subjected to a constant load, viscoelastic materials exhibit a unique response that can be interpreted as having two distinct components. There is an elastic component, which is instantaneous and proportional to the applied load, as well as a gradual, progressive response whose magnitude increases with time, while the rate of increase decays toward zero. Consequently, the behavior of viscoelastic materials can be approximated using conceptual models comprised of simple viscous and elastic elements [30]. A common approach to viscoelastic analysis is to model the material as a generalized Maxwell solid, which contains some combination of springs and dashpots arranged in an array of series and parallel clusters. The resulting model is represented mathematically as a Prony series function, an example of which is given in Eq. (6).

$$E(t) = E_\infty + \sum_{j=1}^{N_p} E_j e^{\left(-\frac{t}{\tau_j}\right)}. \tag{6}$$

Here, E_∞ is the long-term elastic modulus and N_p is the number of Prony terms. The constants E_j and τ_j are calibrated using experimental data in order to fit the model to the actual response of the material with optimal accuracy [31]. The Prony series function describes the *relaxation* process, which is an effect whereby any viscoelastic material subject to a constant applied strain will exhibit a gradual decrease in its internal stress response. In this way, relaxation is the inverse of creep deformation. The relaxation function is alternatively referred to as the *relaxation modulus*. This quantity is the viscoelastic equivalent of Young's modulus in elastic materials.

3.2. The linear viscoelastic model

In the case of a time-varying applied load, the material response will depend on the current load as well as the load rate and the load history. Consequently, viscoelastic materials are sometimes said to have *memory* [32]. Sedef et al. [33] have derived a constitutive relation for modeling the viscoelastic response to an arbitrary load history. Their formulation provides the basis for the model used in the current study.

From the principle of Boltzmann superposition, any linear viscoelastic material can be described using the following stress–strain relationship.

$$\sigma(t) = \int_0^t E(t-s)\frac{\partial \varepsilon(s)}{\partial s}\mathrm{d}s. \tag{7}$$

From Eq. (6), we can resolve the above expression into two components.

$$\sigma(t) = \sigma_0(t) + \sum_{j=1}^{N_p} h_j(t) \tag{8}$$

where $\sigma_0(t) = E_\infty \varepsilon(t)$, and the history parameter, $h_j(t)$, is defined as

$$h_j(t) = \int_0^t E_j e^{\left(-\frac{t-s}{\tau_j}\right)}\frac{\partial \varepsilon(s)}{\partial s}\mathrm{d}s. \tag{9}$$

This quantity is approximated numerically by dividing the time domain into N_t equally-sized discrete time steps, $\Delta t = t_{i+1} - t_i$. The discretized force functions can then be solved using

$$h_j^{(n)} = \sum_{i=1}^{n} e^{\left(-\frac{(n-i)\Delta t}{\tau_j}\right)} A_j \gamma_j \left[\sigma_0^{(i)} - \sigma_0^{(i-1)}\right] \tag{10}$$

where, for conciseness, we have defined the Prony parameters A_j and γ_j as

$$A_j = \frac{\tau_j}{\Delta t}\left(1 - e^{-\frac{\Delta t}{\tau_j}}\right) \quad \text{and} \quad \gamma_j = \frac{E_j}{E_\infty}. \tag{11}$$

3.3. Viscoelastic finite element analysis

When the relaxation modulus is based purely on the axial response of the material, it is referred to as the *extensional* relaxation modulus. When applying this data to the two-dimensional case, a common approach is to assume synchronicity between the shear and bulk moduli [34,33] such that

$$K(t) = \beta G(t) \tag{12}$$

where β is a constant scalar multiplier. Under this assumption, the full viscoelastic response of the material can be captured by a single relaxation modulus [35]. Under this assumption the extensional relaxation modulus, $E(t)$ can be treated as being mathematically equivalent to the time-dependent Young's modulus, E_Y, with Poisson's ratio of the material being constant. The synchronicity assumption has been employed successfully by several authors including Sedef et al. [33] and Schwartz et al. [36]. In the latter study, the authors implemented a three-dimensional numerical model based on axial experimental data by assuming a constant Poisson's ratio, and achieved strong agreement between the experimental and numerical results. Therefore, in the remaining section, we shall simply use the symbol E to refer to both functions. The resulting constitutive matrix for the two-dimensional case is given by

$$\mathbf{C}(t) = \frac{E(t)}{1-\nu^2} \cdot \begin{bmatrix} 1 & \nu & 0 \\ \nu & 1 & 0 \\ 0 & 0 & (1-\nu)/2 \end{bmatrix}. \tag{13}$$

Note that this constitutive matrix corresponds to the plane stress state, which we have assumed for all subsequent derivations and results.

The above equation allows us to directly apply the linear viscoelastic model to a two-dimensional finite formulation, using a slight modification to Eq. (7) so that

$$\boldsymbol{\sigma}(t) = \int_0^t \mathbf{C}(t-s)\frac{\partial \boldsymbol{\varepsilon}(s)}{\partial s}\mathrm{d}s \tag{14}$$

where $\boldsymbol{\sigma}$ and $\boldsymbol{\varepsilon}$ denote the vector representations of the two-dimensional stress and strain tensors respectively (i.e. $\boldsymbol{\sigma} = [\sigma_{xx} \ \sigma_{yy} \ \sigma_{xy}]^{\mathrm{T}}$ etc.). From here we return to Eq. (8), which provides a formula for the internal stress within the material at time t, given its strain history. We can therefore use this expression to derive a corresponding finite element formulation that relates the externally applied forces to the nodal displacements of the structure. We begin with the general equation for total unbalanced internal force, $\mathbf{f}_{\text{int}}$, within each element. This quantity is computed using the following integral evaluated over the volume (denoted as V) of the element.

$$\mathbf{f}_{\text{int}} = \int_{\Omega_e} \mathbf{B}^{\mathrm{T}} \boldsymbol{\sigma} \, \mathrm{d}V \tag{15}$$

where $\mathbf{B}$ is the strain displacement matrix, which is comprised of first-order spatial derivatives of the element shape functions. The matrix relates the nodal displacements of the element, $\mathbf{u}_e$, to the strain tensor via the relation $\boldsymbol{\varepsilon} = \mathbf{B}\mathbf{u}_e$. This equation follows from the kinematic relation ($\boldsymbol{\varepsilon} = \nabla_s \mathbf{u}$), and will form the basis of the governing finite element equations.

For a viscoelastic material, we have defined $\sigma_\infty^{(n+1)}$ such that

$$\boldsymbol{\sigma}_\infty^{(n+1)} = \mathbf{C}_\infty \boldsymbol{\varepsilon}, \tag{16}$$

where $\mathbf{C}_\infty$ is the elasticity tensor evaluated using E_∞ so that $\mathbf{C}_\infty = \mathbf{C}(E_\infty)$. Substituting this expression into Eq. (8), we obtain

$$\begin{aligned}
\boldsymbol{\sigma}^{(n+1)} &= \mathbf{C}_\infty \mathbf{B}\mathbf{u}_e^{(n+1)} + \sum_{j=1}^{N_p} \sum_{i=1}^{n+1} e^{-\frac{t_{n+1}-t_i}{\tau_j}} A_j \gamma_j \left(\mathbf{C}_\infty \mathbf{B}\mathbf{u}_e^{(i)} - \mathbf{C}_\infty \mathbf{B}\mathbf{u}_e^{(i-1)} \right) \\
&= \mathbf{C}_\infty \mathbf{B} \left[\mathbf{u}_e^{(n+1)} + \sum_{j=1}^{N_p} A_j \gamma_j \left[\sum_{i=1}^{n+1} e^{-\frac{t_{n+1}-t_i}{\tau_j}} \left(\mathbf{u}_e^{(i)} - \mathbf{u}_e^{(i-1)} \right) \right] \right].
\end{aligned} \tag{17}$$

We can now return to Eq. (15) and compute the unbalanced internal force at time step $n+1$ as follows.

$$\begin{aligned}
\mathbf{f}_{\text{int}}^{(n+1)} &= \int_{\Omega_e} \mathbf{B}^{\mathrm{T}} \boldsymbol{\sigma}^{(n+1)} \mathrm{d}V \\
&= \mathbf{k}_\infty \mathbf{u}_e^{(n+1)} + \sum_{j=1}^{N_p} A_j \gamma_j \left[\sum_{i=1}^{n+1} e^{-\frac{t_{n+1}-t_i}{\tau_j}} \mathbf{k}_\infty \left(\mathbf{u}_e^{(i)} - \mathbf{u}_e^{(i-1)} \right) \right] \\
&= \mathbf{k}_\infty \left(1 + \sum_{j=1}^{N_p} A_j \gamma_j \right) \mathbf{u}_e^{(n+1)} - \mathbf{k}_\infty \left(\sum_{j=1}^{N_p} A_j \gamma_j \right) \mathbf{u}_e^{(n)} + \sum_{j=1}^{N_p} \mathbf{h}_j^{(n)}.
\end{aligned} \tag{18}$$

Note that here, $\mathbf{k}_\infty = \int_{\Omega_e} \mathbf{B}^{\mathrm{T}} \mathbf{C}_\infty \mathbf{B} \mathrm{d}V$ is the long-term element stiffness matrix, and the history parameter, $\mathbf{h}_j^{(n)}$, for the finite element formulation has the following form.

$$\mathbf{h}_j^{(n)} = A_j \gamma_j \left[\sum_{i=1}^{n} e^{-\frac{(n-i)\Delta t}{\tau_j}} \mathbf{k}_\infty \left(\mathbf{u}_e^{(i)} - \mathbf{u}_e^{(i-1)} \right) \right]. \tag{19}$$

Following the convention of Sedef et al. [33], we can further simplify Eq. (18) by introducing the tangent stiffness matrix, $\mathbf{k}_{\mathrm{T}}$, and the history stiffness matrix $\mathbf{k}_{\text{hist}}$, defined respectively as

$$\mathbf{k}_{\mathrm{T}} = \mathbf{k}_\infty \left(1 + \sum_{j=1}^{N_p} A_j \gamma_j \right) \quad \text{and} \quad \mathbf{k}_{\text{hist}} = \mathbf{k}_\infty \left(\sum_{j=1}^{N_p} A_j \gamma_j \right). \tag{20}$$

Therefore the internal force expression reduces to

$$\mathbf{f}_{\text{int}}^{(n+1)} = \mathbf{k}_{\mathrm{T}} \mathbf{u}_e^{(n+1)} - \mathbf{k}_{\text{hist}} \mathbf{u}_e^{(n)} + \sum_{j=1}^{N_p} \mathbf{h}_j^{(n)}. \tag{21}$$

Note that the latter two terms in the above expression contain previously computed displacement vectors corresponding to past time steps in the forward analysis. For this reason, they are collectively referred to as the *internal force history*, $\mathbf{f}_{\text{hist}}^{(n)}$, and therefore the total internal force can be interpreted as having two components: an instantaneous component given by $\mathbf{k}_{\text{T}}\mathbf{u}_e^{(n+1)}$, and a historical component given by $\mathbf{f}_{\text{hist}}^{(n)}$. Therefore we have

$$\mathbf{f}_{\text{int}}^{(n+1)} = \mathbf{k}_{\text{T}}\mathbf{u}_e^{(n+1)} + \mathbf{f}_{\text{hist}}^{(n)}. \tag{22}$$

From equilibrium, the external (applied) forces must balance the internal forces so that

$$\mathbf{f}_{\text{ext}}^{(n+1)} = \mathbf{f}_{\text{int}}^{(n+1)}. \tag{23}$$

We solve this equation for the current global displacement field $\mathbf{u}^{(n+1)}$, by first assembling global versions of the stiffness matrices and force vectors using

$$\mathbf{K} = \mathop{\mathcal{A}}_{e=1}^{N_e}\mathbf{k}_e; \qquad \mathbf{F} = \mathop{\mathcal{A}}_{e=1}^{N_e}\mathbf{f}_e; \qquad \mathbf{H} = \mathop{\mathcal{A}}_{e=1}^{N_e}\mathbf{h}_e, \tag{24}$$

where N_e represents the total number of elements in the finite element mesh, and $\mathop{\mathcal{A}}_{e=1}^{N_e}$ denotes the assembly operator in which individual element stiffness matrices, force vectors, and force history vectors, denoted as $\mathbf{K}$, $\mathbf{F}$, and $\mathbf{H}$ respectively, are assembled into their global form. Note that the subscript e indicates an element-specific vector or matrix. Also, note that the assembly process can be applied to any of the various stiffness matrices, force vectors and force history vectors defined in the previous section. From here, we solve the discretized global equilibrium equation, which states that the total of all internal and external forces must sum to zero. For time t_{n+1}, this yields

$$\mathbf{K}_{\text{T}}\mathbf{u}^{(n+1)} - \mathbf{F}_{\text{ext}}^{(n+1)} + \mathbf{K}_{\text{hist}}\mathbf{u}^{(n)} + \sum_{j=1}^{N_p}\mathbf{H}_j^{(n)} = \mathbf{0}. \tag{25}$$

Beginning with $\mathbf{u}^{(0)} = \mathbf{0}$ and $\mathbf{H}^{(0)} = \mathbf{0}$, the forward analysis proceeds by successively solving for the current displacement field at each time step as shown above.

Note that in the limit as Δt approaches zero, we have[1]

$$\lim_{\Delta t\to 0} A_j = \lim_{\Delta t\to 0}\left[\frac{\tau_j}{\Delta t}\left(1 - e^{-\frac{\Delta t}{\tau_j}}\right)\right] = 1. \tag{26}$$

Therefore, from Eq. (20), the global tangent stiffness matrix at time $t = 0$ is given by

$$\mathbf{K}_{\text{T}} = \mathbf{K}_\infty\left(1 + \sum_{j=1}^{N_p}\gamma_j\right). \tag{27}$$

Substituting this value into Eq. (25) for time step $n = 0$, we see that the instantaneous response of the structure is equivalent to that of a purely elastic material, whose Young's modulus is the sum of the Prony relaxation coefficients.

$$E_{\text{elastic}} = E_\infty + \sum_{j=1}^{N_p}E_j. \tag{28}$$

4. Sensitivity analysis

Topology optimization problems involve a relatively large number of design variables (typically $n \geq 10^5$), hence gradient-based methods are preferred over evolutionary and population-based approaches. It has been shown that based on current computing technology, the evolutionary methods are prohibitively time- and resource-consuming for most reasonably-sized topology optimization problems [37]. Therefore, we require an efficient and accurate means of

[1] Note that in Eq. (26), we have made use of the identity $\lim_{x\to 0}\frac{1}{x}(a^x - 1) = \ln(a)$, with $x = -\frac{\Delta t}{\tau_j}$ and $a = e$.

computing the design sensitivities, which will guide the optimization search and which form the basis of all gradient-based algorithms. For this task, we employ a time-dependent adjoint formulation, the derivation of which is provided below.

4.1. The time-dependent adjoint method

For a viscoelastic analysis containing N_t time steps, we have $N_t + 1$ residual equations, which correspond to the governing equilibrium equations (Eq. (25)) for each time t_i. Expressing each residual as function of the displacement history, we have

$$\mathbf{R}^{(i)} = \mathbf{R}^{(i)}(\boldsymbol{\rho}, \mathbf{u}^i, \mathbf{u}^{i-1}, \ldots, \mathbf{u}^0) = \mathbf{0} \quad \text{for } i = 0, 1, 2, \ldots, N_t \tag{29}$$

where the global stiffness matrix $\mathbf{K}_\mathrm{T}$ is dependent on the vector of element densities, due to Eq. (5). Based on the above definition, any arbitrary function of interest, f (this may be either an objective or constraint function), can be written as

$$f = f(\boldsymbol{\rho}, \mathbf{u}^{(N_t)}) + \sum_{i=0}^{N_t} \boldsymbol{\psi}^{(i)\mathrm{T}} \mathbf{R}^{(i)}(\boldsymbol{\rho}, \mathbf{u}^i, \mathbf{u}^{i-1}, \ldots, \mathbf{u}^0), \tag{30}$$

where the multipliers, $\{\boldsymbol{\psi}^{(i)}\}$, are a set of vector coefficients that can be chosen to minimize computational expense, since Eq. (30) holds for all values of $\{\boldsymbol{\psi}^{(i)}\}$. To obtain the relevant design sensitivities, we differentiate the above expression with respect to the design variables (in this case, $\boldsymbol{\rho}$).

$$\frac{\mathrm{d}f}{\mathrm{d}\boldsymbol{\rho}} = \frac{\partial f}{\partial \boldsymbol{\rho}} + \frac{\partial f}{\partial \mathbf{u}^{(N_t)}} \frac{\mathrm{d}\mathbf{u}^{(N_t)}}{\mathrm{d}\boldsymbol{\rho}} + \sum_{i=0}^{N_t} \boldsymbol{\psi}^{(i)\mathrm{T}} \left(\frac{\partial \mathbf{R}^{(i)}}{\partial \boldsymbol{\rho}} + \sum_{k=0}^{i} \frac{\partial \mathbf{R}^{(i)}}{\partial \mathbf{u}^{(k)}} \frac{\mathrm{d}\mathbf{u}^{(k)}}{\mathrm{d}\boldsymbol{\rho}} \right). \tag{31}$$

Here, the operator $\frac{\partial a}{\partial b}$ denotes *explicit* derivatives, which only captures a's direct dependence on b. By contrast, the operator $\frac{\mathrm{d}a}{\mathrm{d}b}$ is referred to as an *implicit* derivative since it conveys indirect dependence of a with respect to b, via the governing equations [38]. Consequently, explicit derivatives are significantly less expensive to evaluate than implicit derivatives. Therefore, we must seek a set of values for the coefficients, $\{\boldsymbol{\psi}^{(i)}\}$, that cause all implicit terms to vanish. To do this, we first rearrange Eq. (31) to group similar terms.

$$\frac{\mathrm{d}f}{\mathrm{d}\boldsymbol{\rho}} = \frac{\partial f}{\partial \boldsymbol{\rho}} + \sum_{i=0}^{N_t} \boldsymbol{\psi}^{(i)\mathrm{T}} \frac{\partial \mathbf{R}^{(i)}}{\partial \boldsymbol{\rho}} + \left(\frac{\partial f}{\partial \mathbf{u}^{(N_t)}} + \boldsymbol{\psi}^{(N_t)\mathrm{T}} \frac{\partial \mathbf{R}^{(N_t)}}{\partial \mathbf{u}^{(N_t)}} \right) \frac{\mathrm{d}\mathbf{u}^{(N_t)}}{\mathrm{d}\boldsymbol{\rho}} + \sum_{i=0}^{N_t-1} \left(\sum_{k=i}^{N_t} \boldsymbol{\psi}^{(k)\mathrm{T}} \frac{\partial \mathbf{R}^{(k)}}{\partial \mathbf{u}^{(i)}} \right) \frac{\mathrm{d}\mathbf{u}^{(i)}}{\mathrm{d}\boldsymbol{\rho}}. \tag{32}$$

From here we see that the solution of $\{\boldsymbol{\psi}^{(i)}\}$, which causes all implicit terms to vanish is given by

$$\boldsymbol{\psi}^{(N_t)} = \left[\frac{\partial \mathbf{R}^{(N_t)}}{\partial \mathbf{u}^{(N_t)}} \right]^{-1} \left[-\frac{\partial f}{\partial \mathbf{u}^{(N_t)}} \right]^{\mathrm{T}} \tag{33}$$

$$\boldsymbol{\psi}^{(i)} = \left[\frac{\partial \mathbf{R}^{(i)}}{\partial \mathbf{u}^{(i)}} \right]^{-1} \left[\sum_{k=i+1}^{N_t} -\boldsymbol{\psi}^{(k)\mathrm{T}} \frac{\partial \mathbf{R}^{(k)}}{\partial \mathbf{u}^{(i)}} \right]^{\mathrm{T}}. \tag{34}$$

When solved in this way, the parameters $\{\boldsymbol{\psi}^{(i)}\}$ are referred to as the *adjoint* vectors, and vector $\boldsymbol{\psi}^{(i)}$ represents the adjoint state at time t_i. Substituting the residual expression for each time step, and differentiating with respect to u yield

$$\boldsymbol{\psi}^{(N_t)} = -\mathbf{K}_\mathrm{T}^{-1} \left[\frac{\partial f}{\partial \mathbf{u}^{(N_t)}} \right]^{\mathrm{T}} \tag{35}$$

$$\boldsymbol{\psi}^{(i)} = -\mathbf{K}_\mathrm{T}^{-1} \left[\sum_{k=i+1}^{N_t} \boldsymbol{\psi}^{(k)\mathrm{T}} \left[\delta_{k-1,i} \mathbf{K}_\mathrm{hist} + \sum_{j=1}^{N_p} A_j \gamma_j \left(e^{-\frac{(n-i)\Delta t}{\tau_j}} - e^{-\frac{(n-i+1)\Delta t}{\tau_j}} \right) \mathbf{K}_\infty \right] \right]^{\mathrm{T}}, \tag{36}$$

where δ is the Kronecker delta. In the context of the inverse problem, the adjoint state is analogous to the displacement states computed during the forward problem. Furthermore, the adjoint vectors are solved for in reverse order, as is

typical of adjoint sensitivity analysis for non-linear problems [25]. The solution procedure begins by solving for the adjoint state corresponding to the final time step, t_{N_t}. This vector is then used to solve for the adjoint state of the previous time step, $\boldsymbol{\psi}^{(N_t-1)}$, and so on. Note that the above derivation applies specifically to functions that are dependent only on the final displacement state. However this derivation can easily be extended to functions that are dependent on the full displacement history by modifying each of the equations represented in (34) to include the non-zero terms $\frac{\partial f}{\partial \mathbf{u}^{(i)}}$.

Once we have obtained the full set of adjoint vectors, we can evaluate the sensitivities as follows.

$$\frac{\mathrm{d}f}{\mathrm{d}\boldsymbol{\rho}} = \frac{\partial f}{\partial \boldsymbol{\rho}} + \sum_{i=0}^{N_t} \boldsymbol{\psi}^{(i)\mathrm{T}} \frac{\partial \mathbf{R}^{(i)}}{\partial \boldsymbol{\rho}} \tag{37}$$

where

$$\frac{\partial \mathbf{R}^{(i)}}{\partial \boldsymbol{\rho}} = \left(\mathbf{k}_{\mathrm{T}e}\mathbf{u}_e^{(i)} + \mathbf{k}_{\mathrm{hist}e}\mathbf{u}_e^{(i-1)} + \sum_{j=1}^{N_p} A_j \gamma_j \sum_{k=1}^{i} e^{-\frac{(i-k)\Delta t}{\tau_j}} p\rho_e^{p-1} \mathbf{k}_{\infty e}(\mathbf{u}_e^{(k)} - \mathbf{u}_e^{(k-1)}) \right). \tag{38}$$

Note that here we have made use of the definition of the SIMP penalization function, whose derivative yields the term $p\rho_e^{p-1}$.

In the case of a constant external force, the displacement field becomes a separable function of space and time, (i.e. $\mathbf{u}(t) = \frac{D(t)}{D_0}\mathbf{u}_0$), where $D(t)$ is the creep compliance function, and $D_0 = D(t = 0)$ (a more in depth discussion on this topic is provided in Appendix A.2). Therefore we require only one adjoint vector, which we use to evaluate the implicit sensitivities as follows. For a given function of interest, f, evaluated at time t, we have

$$\frac{\mathrm{d}f(t)}{\mathrm{d}\boldsymbol{\rho}} = \frac{\partial f(t)}{\partial \boldsymbol{\rho}} + \boldsymbol{\psi}^{\mathrm{T}}(t) \frac{\partial \mathbf{R}_0}{\partial \boldsymbol{\rho}}, \tag{39}$$

where $\mathbf{R}_0$ is the residual expression at time $t = t_0$, which yields the elastic solution $\mathbf{u}_0$, and the adjoint vector, $\boldsymbol{\psi}$, is given by

$$\boldsymbol{\psi}(t) = -\frac{D(t)}{D_0} \left[\frac{\partial \mathbf{R}_0}{\partial \boldsymbol{\rho}} \right]^{-1} \frac{\partial f(t)}{\partial \mathbf{u}(t)}. \tag{40}$$

4.2. Computer implementation

The sensitivity analysis along with the forward analysis problem was implemented using Matlab. Table 1 contains a pseudocode description of the algorithm used to compute the sensitivities. Note that the algorithm requires that we store the solution for the displacement field after each time step, so that they may be used in the subsequent adjoint sensitivity analysis. One can avoid having to store the full displacement history by using a direct sensitivity analysis method [9]. In problems involving a large number of time steps, this trade-off may be economically justified, however in most topology optimization problems, this is unlikely to be the case since the number of elements is generally much larger than the number of time steps. For problems requiring adjoint methods, but for which the memory required to store the full solution history of the forward analysis problem (due to a large number of time steps) is prohibitively large, one can employ checkpointing techniques. These algorithms allow for the solution of the adjoint equations, while requiring that users store only those solution states corresponding to a small number of specific time steps known as checkpoints [39,40]. This approach can significantly reduce the memory requirement of the adjoint sensitivity analysis, however it may also increase computation time [39]. The adjoint sensitivity analysis code was verified by comparing the results with those obtained from complex step sensitivity analysis [41].

During each cycle of the optimization process, the analytically computed sensitivities are used to find an optimal update to the current design point. In the current study, this update is determined using the method of moving asymptotes [42], a gradient-based algorithm for solving constrained optimization problems. Fig. 2 contains a schematic diagram illustrating the role of the sensitivity analysis within the larger optimization algorithm. In the figure, the top row of boxes represents operations associated with the forward analysis problem, while the bottom row describes the inverse problem. Each cycle through this loop represents an optimization iteration. The iterative process is repeated until it converges to an optimal design, with optimality being determined by the Karush–Kuhn–Tucker conditions.

Table 1
The time-dependent adjoint sensitivity analysis procedure.

Sensitivity analysis algorithm	
$\frac{\mathrm{d}f}{\mathrm{d}\boldsymbol{\rho}} \leftarrow \frac{\partial}{\partial \boldsymbol{\rho}}[f(\boldsymbol{\rho}, \boldsymbol{u}^{(N_t)})]$	▷ initialize sensitivities
$\boldsymbol{\psi}^{(N_t)} \leftarrow \left[\frac{\partial \mathbf{R}^{(N_t)}}{\partial \mathbf{u}^{(N_t)}}\right]^{-1}\left[-\frac{\partial f}{\partial \mathbf{u}^{(N_t)}}\right]$	▷ solve for final adjoint state
for $i \leftarrow N_t, N_t - 1, \ldots, 0$ **do**:	▷ cycle back through each time step
$\mathbf{F}_{\mathrm{RHS}} \leftarrow \mathbf{0}$	▷ initialize right-hand-side vector
# Cycle forward through all subsequent time steps	
for $k \leftarrow i+1, i+2, \ldots, N_t$ **do**:	
$\mathbf{F}_{\mathrm{RHS}} \leftarrow \mathbf{F}_{\mathrm{RHS}} - \left[\boldsymbol{\psi}^{(k)} \frac{\partial \boldsymbol{R}^{(k)}}{\partial \boldsymbol{u}^{(i)}}\right]$	
end for	
$\boldsymbol{\psi}^{(i)} \leftarrow \left[\frac{\partial \boldsymbol{R}^{(i)}}{\partial \boldsymbol{u}^{(i)}}\right]^{-1} \mathbf{F}_{\mathrm{RHS}}$	▷ solve for intermediate adjoint vectors (Eq. (36))
$\frac{\mathrm{d}f}{\mathrm{d}\boldsymbol{\rho}} \leftarrow \frac{\mathrm{d}f}{\mathrm{d}\boldsymbol{\rho}} + \boldsymbol{\psi}^{(i)} \frac{\partial \boldsymbol{R}^{(i)}}{\partial \boldsymbol{\rho}}$	▷ add adjoint terms
end for	

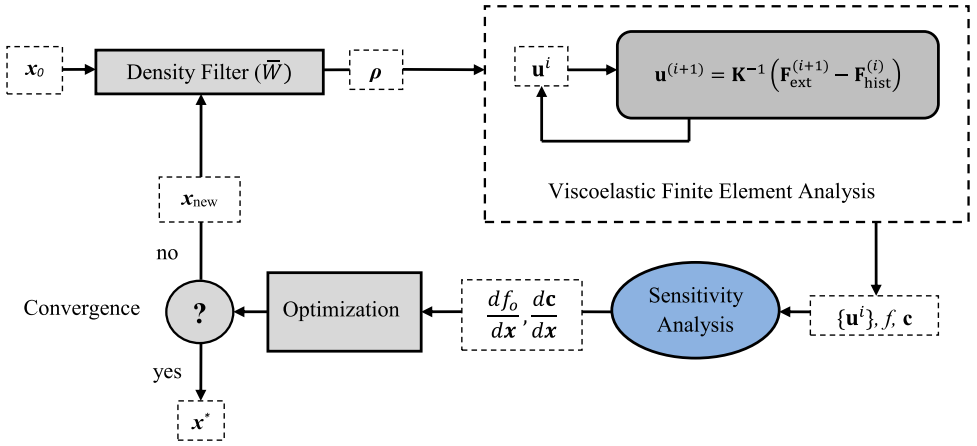

Fig. 2. Data flow and order of operations during the optimization procedure.

Incorporating viscoelasticity into the topology optimization algorithm can significantly increase the computational cost of the design optimization procedure. The severity of this increase is primarily dependent on the time discretization and the number of time steps used in the viscoelastic analysis. In both the viscoelastic topology optimization algorithm and the standard topology optimization algorithm, the most costly operation is the solution of the residual (structural equilibrium) equations, and the solution of the adjoint equations, each of which requires the factorization of the tangent stiffness matrix, or in the case of large-scale problems, the solution of a large linear system via iterative methods. In both cases, the size of the system that must be solved is given by the number of degrees of freedom in the finite element mesh. In the viscoelastic algorithm, these operations must be carried out for once for each time step in the structural analysis. The number of time steps must be large enough to accurately capture the full load history using discrete data points. The incremental cost of additional time steps is independent of the size and geometry of the structure, which itself contributes to the cost of the algorithm, as this determines the size of the tangent stiffness matrix.

5. Numerical examples

In the sections that follow, the viscoelastic optimization techniques described above are demonstrated on a series of two-dimensional examples problems. In the first set of examples, the geometry and boundary conditions are based on the Messerschmitt–Bölkow–Blohm (MBB) beam, shown in Fig. 3. An MBB beam of this size could be used as a support structure for temporary deployable bridges, which are commonly used by military personnel. Other applications include the design of floor supports for the fuselage of an aircraft. In both cases, a light-weight design confers

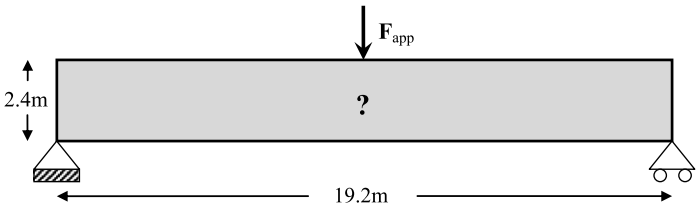

Fig. 3. Geometry and boundary conditions for the viscoelastic MMB beam problem (the depth of the structure in the direction going into the page is 0.1 m).

significant advantages. The design objective is to minimize the mass of the structure, subject to a constraint on the final midpoint deflection at the location of the applied load. The optimization problem is stated mathematically below.

$$\begin{aligned}
&\min_{\boldsymbol{\rho}} \sum_{e=1}^{N_e} \rho_e V_e \\
&\text{subject to : } \mathbf{L}^{\mathrm{T}}\mathbf{u}^{(N_t)} \leq \mathrm{def}_{\max} \\
&\qquad \mathbf{K}_{\mathrm{T}}\mathbf{u}^{(i+1)} - \mathbf{F}_{\mathrm{ext}}^{(i+1)} + \mathbf{K}_{\mathrm{hist}}\mathbf{u}^{(i)} + \sum_{j=1}^{N_p} \mathbf{H}_j^{(i)} = \mathbf{0}, \quad i = 1, 2, \ldots, N_t \\
&\qquad 0 < \rho_{\min} \leq \rho_i \leq 1, \quad i = 1, 2, \ldots, N_e,
\end{aligned} \tag{41}$$

where $\mathbf{L}$ is the unit basis vector, whose entries are all zeros except in the location corresponding to the degree of freedom at which the vertical midpoint deflection is measured, and $\mathrm{def}_{\max}$ is the maximum allowable midpoint deflection of the structure. Note also that $\rho_{\min}$ is a small lower bound chosen to avoid singularities in the global stiffness matrix. In the results presented, we used a value of $\rho_{\min} = 10^{-3}$.

In all the examples presented, the structures are comprised of polypropylene, a versatile and widely used polymer known for its low density and high stiffness. To model the material, we use a five-term Prony series expansion, whose coefficients are given in Table A.2. Appendix contains a detailed discussion on the procedure used to obtain the Prony series terms used in this study.

5.1. Gravitational loading

Loading due to the self-weight of the structure is a common cause of creep deformation, since these loads are constant and sustained over the entire lifespan of the structure. In the case of civil infrastructure, loading due to self-weight may also be significantly larger in magnitude than the various temporary loads the structure may encounter. In the following example we include a gravitational body force, which is based on the volumetric mass density of polypropylene ($\rho_{V_e} = 946\ \mathrm{kg/m^3}$) and an acceleration due to gravity of $a_g = -9.81\ \mathrm{m/s^2}$. Because the force is constant, we use the creep compliance function to obtain the displacement fields at any given time, t (see Appendix A.2 for the derivation of the creep-compliance function used in the numerical examples below).

In addition to the gravitational force, we also include a fixed applied load at the midpoint of the top surface of the beam. This fixed load prevents the optimizer from converging to the trivial solution in which all material is fully removed from the structure, which would effectively minimize the external force. The fixed load is also useful since it represents temporary loading, which the structure must also withstand in addition to its own weight.

Therefore, for the gravitational loading problem, the external force vector is computed using the following sum.

$$\mathbf{F}_{\mathrm{ext}} = \mathbf{F}_{\mathrm{app}} + \mathbf{F}_g, \tag{42}$$

where $\mathbf{F}_{\mathrm{app}}$ is a concentrated load applied to the center of the beam's top surface, and the gravitational force, $\mathbf{F}_g$ is computed as the sum of the gravitational body forces acting on each element, $\mathbf{f}_{g_e}$, as shown in Eq. (44),

$$\mathbf{F}_g = \mathcal{A}_{e=1}^{N_e} \mathbf{f}_{g_e}, \tag{43}$$

$$\mathbf{f}_{g_e} = \rho_V a_g \int_{\Omega_e} \mathbf{N}_s \rho_e \mathrm{d}V, \tag{44}$$

(a) Elastic design; Mass = 888 kg.

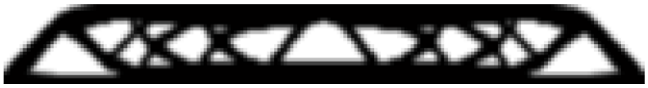

(b) Worst-case design; Mass = 2780 kg.

(c) Viscoelastic design; Mass = 1571 kg.

Fig. 4. MBB beam designs optimized for the elastic case (a), the worst case (b), and for a 2500 s viscoelastic analysis (c).

where $\mathbf{N}_s$ is the vector of shape functions associated with element e. Also note that ρ_V is the volumetric mass density of the bulk material, and a_g is the acceleration due to gravity, both of which are constant throughout the design domain. Due to the gravitational term, the external force is design-dependent, and therefore, the explicit derivative of the residual is computed using

$$\frac{\partial \mathbf{R}}{\partial \boldsymbol{\rho}} = \frac{\partial (\mathbf{K}_{\mathrm{T}}\mathbf{u})}{\partial \boldsymbol{\rho}} - \frac{\partial \mathbf{F}_g}{\partial \boldsymbol{\rho}} + \frac{\partial \mathbf{F}_{\mathrm{hist}}}{\partial \boldsymbol{\rho}}. \tag{45}$$

Note that in all problems involving constant loading (as is the case with gravitational loads), the full displacement history can be computed based on a single linear analysis using the creep compliance function. Therefore, during each forward analysis problem, we need to solve only one residual equation. Similarly, for constant-load problems, we require the solution of only one adjoint vector (defined in Eq. (40)), which greatly reduces the computational cost of the algorithm. The full mathematical procedure for obtaining the creep compliance function, and performing the corresponding structural analysis is described in detail in Appendix A.2.

In the examples presented, the applied point load had a magnitude of 21 kN, which accounted for approximately one half to two thirds of the total force acting on each structure. We assume a constant temperature of 23 °C. For each solution, the maximum allowable midpoint deflection was constrained to 27 cm.

5.1.1. Viscoelastic design vs. linear elastic design

In the absence of a time-dependent viscoelastic finite element model and the corresponding sensitivity analysis capability, one can design for either the worst case ($E = E_\infty$) or for the purely elastic case ($E = E_0$), conduct a linear elastic analysis using a constant elasticity modulus. Fig. 4 shows the optimized designs obtained using linear analyses based on the worst case and the elastic case, as well as an optimized design based on a viscoelastic analysis corresponding to constant gravitational and applied loads. The viscoelastic design is optimized for a load duration of 2500 s.

Fig. 5 shows the creep plots for each of the three designs over the specified time period. While the deflection of the viscoelastic design meets the design constraint exactly, the designs obtained from linear elastic analysis either overshoot or undershoot the target deflection. In the plots, the initial deflection at $t = 0$ represents the elastic portion of the deformation, which occurs instantaneously once the load is applied. The subsequent deflection is due to creep. Note that the initial deflection of the elastic design is equal to the maximum deflection as expected. Similarly, if the plots were extended to $t = \infty$, the deflection plot for the worst-case design would asymptotically approach the maximum deflection barrier.

In case of the elastic design, we have overestimated the stiffness of the structure by assuming purely elastic behavior. This leads to an insufficiently stiff structure when analyzed using full viscoelastic analysis, thereby causing structure to breach the design requirements. By contrast, the worst-case design is overly conservative. While the design does satisfy the desired deflection requirement, it is significantly heavier than the viscoelastic design, and is therefore suboptimal.

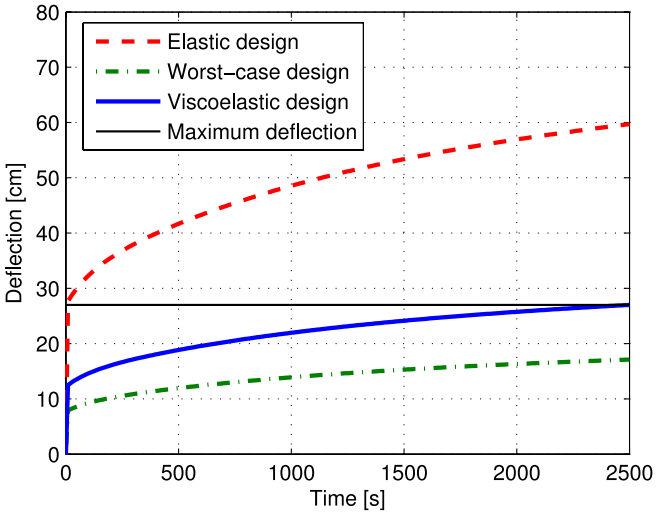

Fig. 5. Creep histories of the three structures optimized using elastic, worst-case and viscoelastic analysis.

(a) $t^* = 2500$ s; Mass = 1571 kg.

(b) $t^* = 6000$ s; Mass = 1944 kg.

(c) $t^* = 15\,000$ s; Mass = 2333 kg.

Fig. 6. MBB beam designs optimized for various time durations.

5.1.2. Targeted design

In contrast to the above examples, below we solve the same gravitational loading problem described above, using multiple time-dependent viscoelastic optimizations. In this way, we obtain specialized designs that are optimized for a specific load duration. In order to simulate the expected operation time or life cycle of the structure, the design problem was solved for time durations of 6000 and 15 000 s, in addition to the 2500 s solution presented above. Fig. 6 shows the optimized designs for each of the three durations. As the results indicate, the structures that are designed to operate and withstand applied load for longer durations, undergo greater creep, and therefore, the mass of the structure must be increased, thus reducing the elastic deformation, to compensate for the increased creep deformation. Consequently, the three structures, although designed for the same applied loading and boundary conditions, differ significantly in their design. Fig. 7, shows the deformed structure of Fig. 6(a), illustrating the combined effect of creep and elastic deformation.

As demonstrated in Fig. 6, the duration of the load for which the structure is designed has a major impact on the mass of the optimal structure. Fig. 8 displays the masses of various optimized structures plotted versus the duration of the constant load for which each structure was optimized. Each circular point on the plot, represents a unique solution to the constant-load optimization problem. As expected, the plot follows a path that is similar to that of the creep compliance function, with longer load durations requiring heavier, and therefore stiffer, structures. For long load durations,

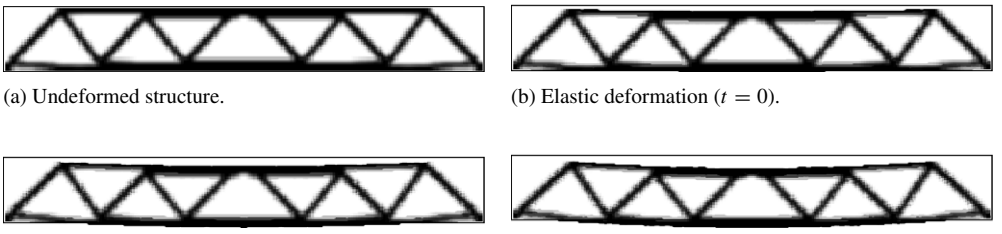

(a) Undeformed structure.

(b) Elastic deformation ($t = 0$).

(c) Viscoelastic deformation ($t = 2500$ s).

(d) Viscoelastic deformation ($t = 15\,000$ s).

Fig. 7. Creep deformation due to various load durations (note: the solid black line represents the boundary of the working domain).

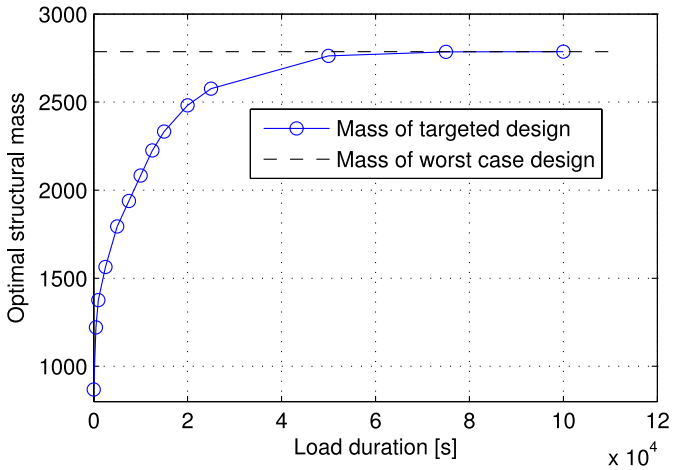

Fig. 8. Masses of various optimized structures plotted versus the duration of the constant load for which each structure was designed.

the final deflection of the structure approaches the worst-case deflection. Therefore, designers must determine whether the mass savings yielded by targeted viscoelastic design optimization are sufficient to justify the computational cost of the procedure. In some cases, designers may choose to simply design for the worst-case deflection in order to save time and computational resources.

5.2. Time-dependent loading

5.2.1. Intermittent loading

For the first time-dependent loading example, we retain the problem geometry and boundary conditions of the MBB beam described in Fig. 3. However, we replace the constant applied load with a intermittent series of intermittent loads, whose magnitudes follow a repeating step pattern, (see Fig. 9). This problem was previously investigated by Grossman and Takai [43,44] in their studies on the deflection of wood under intermittent loading. Here it was observed that the final viscoelasticity of the wood caused a cumulative impact on the structural response, which depended on the number, duration, magnitude and frequency of the load steps.

In the examples presented, we have decreased the length scale of the previous problem by a factor of 10, so that the working domain measures 1.92 m across and 0.24 m vertically. This particular problem has applications to the design of roof trusses for small temporary shelters, many of which are comprised of polymers, which exhibit viscoelastic behavior. The depth of the structure in the direction perpendicular to the page is 1 cm. As in the previous example, the structure is comprised of polypropylene, with the material parameters chosen from experimental data taken at room temperature (23 °C). We optimize the structure for two different intermittent loading patterns, whose time history is provided in Fig. 9. The analysis for load history #1 was carried out using 25 time steps, while the analysis for load history #2 was carried out using 28 time steps. Additionally, we performed a third optimization for the *worst case* in which we assumed an infinite loading duration, (i.e. constant load with $D = D_\infty$). For all three load histories, the maximum allowable midpoint deflection was constrained to 0.15 m. In all cases, we assume that, although the

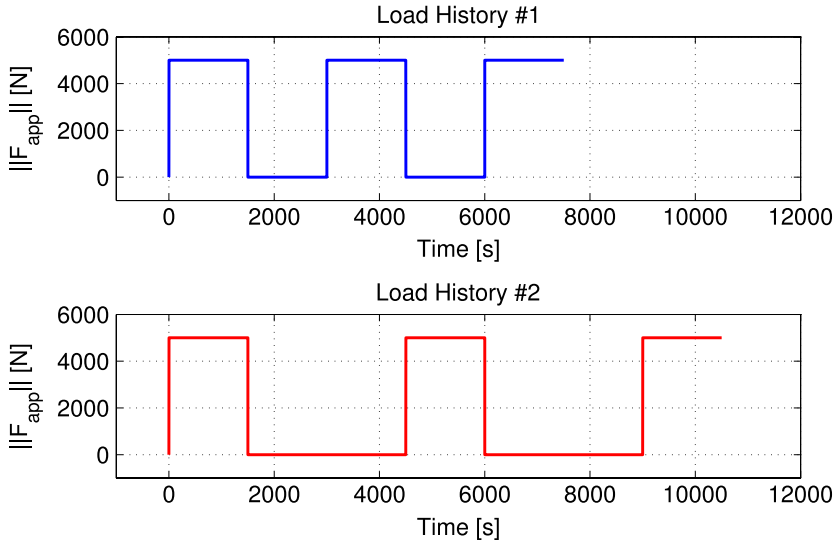

Fig. 9. Intermittent load histories for the two sample problems.

(a) Load history #1; Mass = 1.76 kg.

(b) Load history #2; Mass = 1.69 kg.

(c) Worst case load history; Mass = 2.57 kg.

Fig. 10. MBB beam designs optimized for various intermittent load histories.

applied load is time-dependent, the analysis is quasi-static (i.e. no inertial effects), since the time scale is very large and all accelerations are negligible. In these examples, we also ignore the effect of self-weight, which we assume to be negligible when compared to the applied load.

Fig. 10 shows the optimized designs corresponding to the two intermittent load histories as well as the worst case load history. Note that in both intermittent loading scenarios, the load has the same magnitude and is applied for a total of 4500 s. However, in scenario 2, the recovery period is twice as long, which results in a smaller final deflection. Consequently, design (b) is lighter than design (a), since its viscoelastic recovery period allows for larger elastic deflections. Similarly, if one fails to take into account the full load history, and instead designs only for the worst case, the design will be overly conservative, and the designers will forgo potential weight savings. Fig. 11, shows the creep plots of the optimized designs caused by their respective loading histories.

5.2.2. Strain-rate loading

In the final set of example problems we apply point loads whose magnitudes increase linearly with time, and examine the impact of the load rate on the optimal design. For this example, we optimize the cantilever beam, whose geometry and boundary conditions are shown in Fig. 12. The optimization problem was solved for three different load histories, in which the load magnitudes increase linearly at varying rates. Fig. 13, contains plots of the load three load

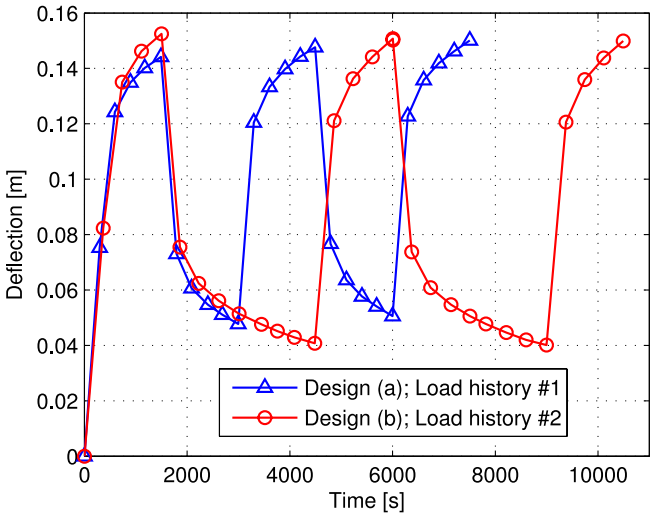

Fig. 11. Creep histories for designs (a) and (b) of Fig. 10, caused by their respective load histories; In both plots, the maximum allowable deflection was constrained to 0.15 m.

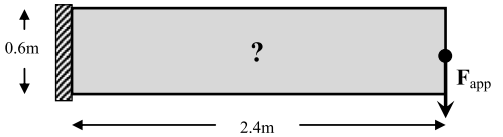

Fig. 12. Geometry and boundary conditions for the viscoelastic cantilever beam problem (the depth of the structure in the direction going into the page is 2.5 cm).

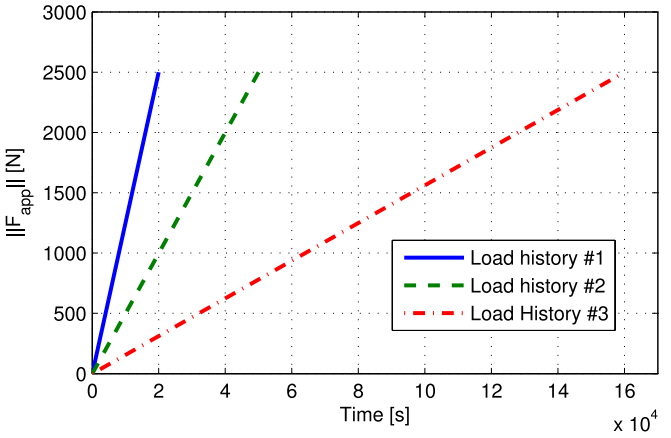

Fig. 13. Linearly varying load histories.

histories implemented. For each load history, the time-dependent viscoelastic finite element analysis was carried out using 10 time steps.

The optimized structures corresponding to each load history is shown in Fig. 14. For completeness, we have also included plots of the convergence histories of the objective function (in this case, mass) for each of the three optimizations (see Fig. 15). As was the case with the gravitational loading example, the structures subject to longer loading durations have greater mass in order to increase their elastic stiffness. The difference in mass results in noticeable topological differences in the three designs. This ability to tailor the design of the structure to accommodate specific load rates, is an advantage of viscoelastic design, which is absent in linear elastic methods, since the elastic deflection depends only on the final load magnitude and is independent of the load rate.

(a) Load history #1; Mass = 15.19 kg. (b) Load history #2; Mass = 17.26 kg. (c) Load history #3; Mass = 19.07 kg.

Fig. 14. MBB beam designs optimized for various intermittent load histories.

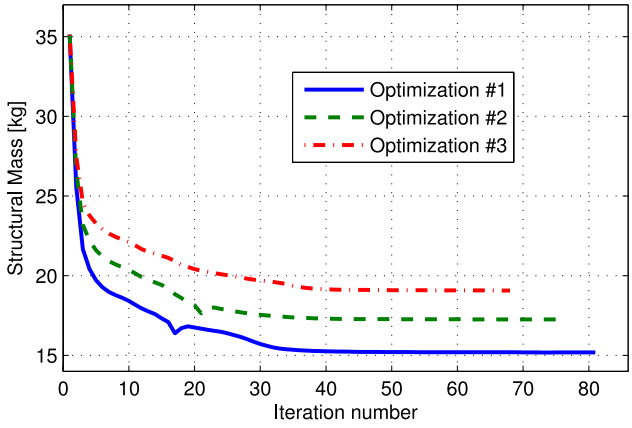

Fig. 15. Convergence plots for the optimizations corresponding the three linearly varying load histories in Fig. 13.

6. Conclusions

We have presented an original algorithm for performing topology optimization of viscoelastic structures using a time-dependent adjoint method, which we have derived and implemented. The method was used to optimize a series of structures subject to sustained loading in order to achieve optimal structural performance over prolonged operating periods. Each structure was optimized for minimum mass subject to a constraint on the maximum allowable deflection at the end of the loading period. In the case of constant loading, it was demonstrated that the design of the optimal structure is highly dependent on the duration of the applied load and the time at which the deflection is measured. In the case of time-varying load, the optimal design was again dependent on the duration and pattern of the load history. By simulating the full viscoelastic response for all time ($0 < t \leq t_{\text{final}}$) one is able to obtain an accurate measure of the final structural response. In this way, the method allows us to exploit the full feasible design envelope, which can result in significant weight savings. By contrast, we have shown that optimized designs based on linear analysis are suboptimal, and can lead to infeasibility (in the case of assumed linear elasticity) or an unnecessarily heavy structure (in the case of the worst-case assumption with constant loading). The capabilities provided by viscoelastic design are particularly useful for the design of aging structures, as well as structures that are subject to sustained loading, where viscoelastic effects become dominant, and can negatively impact the performance of the design.

Acknowledgment

The authors wish to acknowledge the financial support of the National Science Foundation under grant CMMI-1334857.

Appendix. Material parameters

A.1. The relaxation function

In the current study, the assigned material parameters are based on the measured properties of polypropylene, an industrial polymer used in a wide variety of engineering applications including containers, packaging, and automotive interior parts. Polypropylene has several properties, which make it desirable for engineering design and manufacturing. Among these are its high stiffness (including at high temperatures), and its light weight. The material properties vary

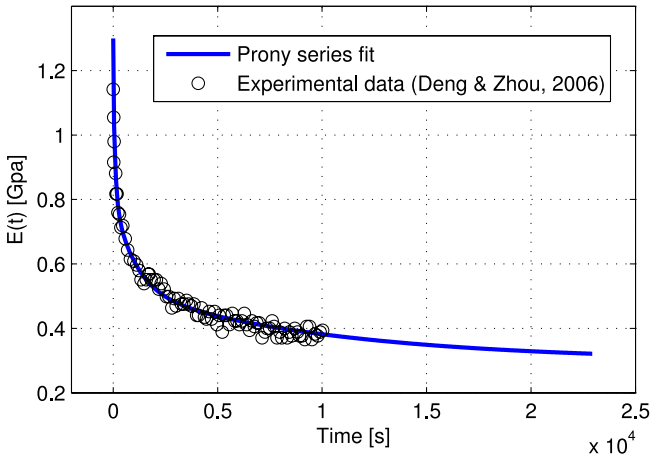

Fig. A.16. Experimental relaxation data and its corresponding Prony series function for polypropylene at room temperature 23 °C.

according to the method of production and the co-polymers used, however we have selected relevant sample data from published studies for use in the examples presented.

Like all polymers, polypropylene exhibits significant viscoelastic behavior, which has been investigated extensively in the literature [45–48]. In order to obtain a Prony series expression for the relaxation modulus, we perform a least squares fit of the experimental data reported by Deng and Zhou [49]. In their 2006 study, they measured the stress relaxation of polypropylene specimens used for medical sutures. The data were obtained from axial loading tests, which were performed at various temperatures. For the current study, we have chosen the experimental data corresponding to a 13% strain applied at room temperature (23 °C).

In order to fit the data, we assume a 5-term Prony series solution of the form given in Eq. (6). The experimental data are provided for times ranging from 0 to 10^4 s, therefore we select the retardation times, $\{\tau_j\}$, using decade intervals so that they span the desired time domain (i.e. $\{\tau_j\} = \{10, 100, 1000, 10000\}$), in accordance with the power law procedure proposed by Park and Kim [31]. We then selected an evenly distributed sampling of N_{exp} data points, $\{t_i, \sigma_i\}$, from the experimental data. Combining the experimental data with our assumed Prony Series expression, we obtain N_{exp} equations of the form

$$E(t_i) = E_\infty + \sum_{j=1}^{N_p-1} E_j e^{\frac{t_i}{\tau_j}} \approx E_{\text{exp}_i}, \quad \text{for } i = 1, 2, \ldots, N_{\text{exp}}. \tag{A.1}$$

Note that since the strain is constant ($\varepsilon = 0.13$), the experimental relaxation moduli, $\{E_{\text{exp}_i}\}$ are computed using $E_{\text{exp}_i} = \sigma_i/\varepsilon$. Eq. (A.1) results in a linear system of equations that can be written as

$$\mathbf{C}_E\mathbf{E} \approx \mathbf{E}_{\text{exp}}, \tag{A.2}$$

where $\mathbf{C}_E$ is a known $N_{\text{exp}} \times N_p$ matrix, and $\mathbf{E}$ is the vector of relaxation coefficients, $[E_\infty, E_1, E_2, \ldots, E_{N_p-1}]^{\mathbf{T}}$. Note that the number of experimental data point exceeds the number of Prony series terms. Therefore, the least squares solution for $\mathbf{E}$ is given by

$$\min_{\mathbf{E}} \|\mathbf{C}_E\mathbf{E} - \mathbf{E}_{\text{exp}}\|_2$$
$$\Rightarrow \mathbf{E} = [\mathbf{C}_E^{\mathbf{T}}\mathbf{C}_E]^{-1}\mathbf{C}_E^{\mathbf{T}}\mathbf{E}_{\text{exp}}. \tag{A.3}$$

Fig. A.16 shows a plot of the experimental data alongside the corresponding Prony series function used to fit the data. In the examples presented, Poisson's ratio is assumed to be constant with a value of $\nu = 0.45$.

A.2. The creep compliance function

In the special case where the external force is constant, the structure undergoes pure creep. For a structure comprised of isotropic material subject to small displacements, the internal stresses remain constant. Therefore it is possi-

ble to derive a closed-form expression for the structural displacements at any time $t > 0$ using the creep compliance function. The creep compliance function is an intrinsic property of the material, and can be interpreted as the inverse of the relaxation modulus since it describes the strain history over time for a given constant applied stress. Like the relaxation modulus, the creep deformation function can be approximated using a Prony series to fit experimental data. However, in many cases the only experimental data available are for relaxation rather than creep. For this reason authors have developed various techniques for obtaining the creep compliance function either directly from experimental relaxation data [50], or by deriving it analytically from the relaxation modulus [30,51,52]. In the current study, we employ a direct numerical method, the derivation of which is presented below.

For a linear, viscoelastic material, from Boltzmann superposition we have the following relation.

$$\varepsilon(t) = \int_0^t D(t-s)\frac{\partial \sigma(s)}{\partial s}\mathrm{d}s \tag{A.4}$$

where $D(t)$ is the creep compliance (note the similarity with Eq. (7), which describes the analogous relation for the relaxation function). Now suppose one were to apply an axial stress that precisely mimics the relaxation functions so that $\sigma(t) = E(t)$, where $E(t)$ is the relaxation modulus. This would be equivalent to the relaxation test, therefore the result would be a constant unit strain, $\varepsilon(t) = 1$.

$$\int_0^t D(t-s)\frac{\partial E(s)}{\partial s}\mathrm{d}s = 1. \tag{A.5}$$

Integrating the above equation, we get

$$\int_0^t D(t-s)E(s)\mathrm{d}s = t, \quad \text{for } t > 0 \tag{A.6}$$

from this expression it may be possible to analytically derive the creep compliance function $D(t)$, based on the closed-form Prony series expression for the relaxation modulus, $E(t)$. However, in practice an analytical solution may not exist, thus it is more common to solve the problem numerically using retardation spectra [53].

In order to obtain a creep compliance function, we assume a Prony series solution of the form

$$D(t) = D_\infty - \sum_{j=1}^{N_p-1} D_j e^{-t/\tau_j}, \tag{A.7}$$

where we again set the retardation times $\{\tau_j\}$ to [10, 100, 1000, 10 000] (note that in the examples presented, we use a 5-term Prony series, as was the case with the relaxation modulus). Using the experimental data shown in Fig. A.16, we have $N_{\text{exp}} - 1$ equations with which to find a least squares solution for the creep compliance coefficients, $\{D_\infty, D_1, D_2, \ldots, D_{N_p-1}\}$. From Eq. (A.6), for each experimental data point t_i we have

$$\int_0^{t_i} D(t_i-s)E(s)\mathrm{d}s = t_i, \quad \text{for } i = 1, 2, \ldots, N_{\text{exp}} - 1. \tag{A.8}$$

Following the procedure proposed by Liu [50], we approximate these integrals using a trapezoidal quadrature rule using the experimental data points, $\{E_{\text{exp}_i}\}$.

$$\sum_{k=1}^{i}\frac{1}{2}(t_k - t_{k-1})\left[E_{k-1}\left(D_\infty - \sum_{j=i}^{N_p-1} D_j e^{-\frac{t_i - t_{k-1}}{\tau_j}}\right)\cdots + E_k\left(D_\infty - \sum_{j=i}^{N_p-1} D_j e^{-\frac{t_i - t_k}{\tau_j}}\right)\right] \approx t_i, \quad \text{for } i = 1, 2, \ldots, N_{\text{exp}} - 1. \tag{A.9}$$

Simplifying this equation results in the following linear algebraic system.

$$\mathbf{C}_D\mathbf{D} \approx \mathbf{T}_{\text{exp}}, \tag{A.10}$$

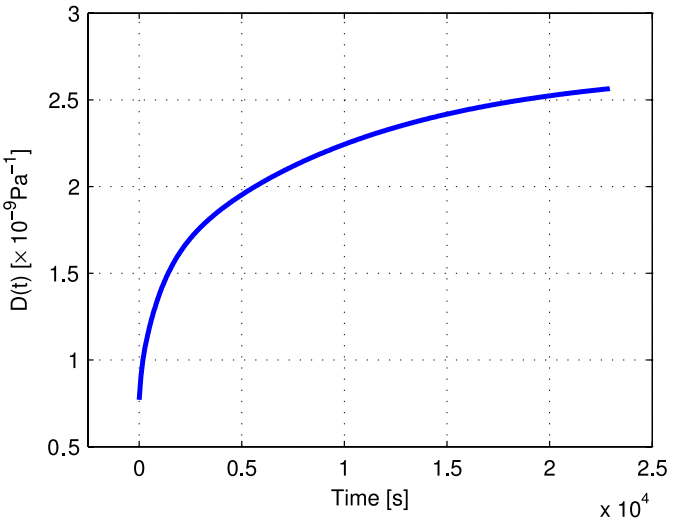

Fig. A.17. Prony series creep compliance function based on experimental relaxation data for polypropylene at room temperature (23 °C) [49].

Table A.2
Prony series coefficients used in the relaxation and creep compliance functions.

Relaxation (GPa)		Creep compliance (GPa^{-1})		Retardation times (s)	
E_0	0.2983	D_0	2.6859	–	–
E_1	0.1255	D_1	0	τ_1	10
E_2	0.3645	D_2	0.1311	τ_2	100
E_3	0.2844	D_3	0.5825	τ_3	1 000
E_4	0.2273	D_4	1.2031	τ_4	10 000

where $\mathbf{C}_D$ is a known $(N_{\text{exp}} - 1) \times N_p$ matrix, $\mathbf{D}$ is the vector of creep compliance coefficients, $[D_\infty, D_1, D_2, \ldots, D_{N_p-1}]^{\text{T}}$, and $\mathbf{T}_{\text{exp}}$ is the vector of experimental data point times, excluding t_0. In order to ensure that all coefficients are non-negative, we have solved the above problem using the nonnegative linear least squares method [54]. Fig. A.17 contains a plot of the Prony series function obtained from the experimental data shown in Fig. A.16.

For a fully isotropic structure subject to small displacements, we can use the creep compliance function to solve for the displacements at any time t using

$$\mathbf{u}(t) = \mathbf{u}_0 \frac{D(t)}{D_0}, \tag{A.11}$$

where D_0 is the instantaneous (elastic) compliance, given by

$$D_0 = D(0) = D_\infty - \sum_{j=1}^{N_p-1} D_j, \tag{A.12}$$

and $\mathbf{u}_0$ is the elastic displacement obtained from the solution of

$$\mathbf{R}_0 = \mathbf{K}(E_0)\mathbf{u}_0 - \mathbf{F}_{\text{ext}} = \mathbf{0}. \tag{A.13}$$

Here, the external force vector, $\mathbf{F}_{\text{ext}}$, is constant with respect to time, and the global stiffness matrix, $\mathbf{K}$, is computed using the elasticity modulus, $E_0 = 1/D_0$. Table A.2 contains the values for the Prony coefficients (for both relaxation and creep compliance) obtained from the above-described procedures when applied to the experimental data shown in Fig. A.16.

References

[1] M.P. Bendsøe, N. Kikuchi, Generating optimal topologies in structural design using a homogenization method, Comput. Methods Appl. Mech. Engrg. 71 (1988) 197–224.
[2] M.P. Bendsøe, Optimal shape design as a material distribution problem, Struct. Optim. 1 (1989) 193–202.
[3] J. Betten, Creep Mechanics, Springer, 2005.
[4] R. Mayer, N. Kikuchi, R. Scott, Applications of topological optimization to structural crashworthiness, Internat. J. Numer. Methods Engrg. 15 (1996) 1383–1403.
[5] C. Pederson, Crashworthiness design of transient frame structures using topology optimization, Comput. Methods Appl. Mech. Engrg. 193 (2004) 653–678.
[6] J. Forsberg, L. Nilsson, Topology optimization in crashworthiness design, Struct. Multidiscip. Optim. 33 (2007) 1–12.
[7] C. Olschinka, A. Schumacher, Graph based topology optimization of crashworthiness structures, Proc. Appl. Math. Mech. 8 (2008) 10029–10032.
[8] N. Patel, A. Tovar, B. Kang, J. Renaud, Crashworthiness design using topology optimization, J. Mech. Des. 31 (2009) 1–12.
[9] C. Swan, I. Kosaka, Voight–Reuss topology optimization for structures with nonlinear material behaviors, Internat. J. Numer. Methods Engrg. 40 (1997) 3785–3814.
[10] K. Maute, S. Schwartz, E. Ramm, Adaptive topology optimization of elastoplastic structures, Struct. Optim. 15 (1998) 81–91.
[11] L. Kachanov, Time of the rupture process under creep conditions, Izv. Akad. Nauk SSSR. Otdel. Tekhnicheskich Nauk 8 (1958) 26–31.
[12] B. Desmorat, R. Desmorat, Topology optimization in damage governed low cycle fatigue, C. R. Mech. 336 (2008) 448–453.
[13] O. Amir, A topology optimization procedure for reinforced concrete structures, Comput. & Structures 114–115 (2012) 46–58.
[14] O. Amir, O. Sigmund, Reinforcement layout design for concrete structures based on continuum damage and truss topology optimization, Struct. Multidiscip. Optim. 47 (2012) 157–174.
[15] K. James, H. Waisman, Failure mitigation in optimal topology design using a coupled nonlinear continuum damage model, Comput. Methods Appl. Mech. Engrg. 268 (2014) 614–631.
[16] J. Prasad, A. Diaz, Viscoelastic material design with negative stiffness components using topology optimization, Struct. Multidiscip. Optim. 38 (2009) 583–597.
[17] E. Andreassen, J. Jensen, Topology optimization of periodic microstructures for enhanced dynamic properties of viscoelastic composite materials, Struct. Multidiscip. Optim 49 (5) (2014) 695–705.
[18] A. El-Sabbagh, A. Baz, Topology optimization of unconstrained damping treatments for plates, Eng. Optim 46 (9) (2014) 1153–1168.
[19] Z. Liu, H. Guan, W. Zhen, Topology optimization of viscoelastic materials distribution of damped sandwich plate composite, Appl. Mech. Mater. 347–350 (2013) 1182–1186.
[20] W. Chen, S. Liu, Topology optimization of microstructures of viscoelastic damping materials for a prescribed shear modulus, Struct. Multidiscip. Optim. http://dx.doi.org/10.1007/s00158-014-1049-3.
[21] K. Jensen, P. Szabo, F. Okkels, Topology optimization of viscoelastic rectifiers, Appl. Phys. Lett. 100 (2012) 1–4.
[22] M. Zhou, G.I.N. Rozvany, The COC algorithm, part II: topological, geometrical and generalized shape optimization, Internat. J. Numer. Methods Engrg. 37 (1991) 2471–2499.
[23] O. Sigmund, J. Peterson, Numerical instabilities in topology optimization: a survey on procedures dealing with checkerboards, mesh-dependencies and local minima, Struct. Optim. 16 (1998) 68–75.
[24] C.S. Jog, R.B. Haber, Stability of finite element models for distributed parameter optimization and topology design, Comput. Methods Appl. Mech. Engrg. 130 (1996) 203–226.
[25] T.E. Bruns, D.A. Tortorelli, Topology optimization of non-linear elastic structures and compliant mechanisms, Comput. Methods Appl. Mech. Engrg. 190 (26–27) (2001) 3443–3459.
[26] J. Plumbridge, Materials (Special Issue), Open Access, 2012.
[27] R. Duddu, H. Waisman, A nonlocal continuum damage mechanics approach to simulation of creep fracture in ice sheets, Comput. Mech. 51 (6) (2013) 961–974.
[28] S. Murakami, Notion of continuum damage mechanics and its application to anisotropic creep damage theory, Trans. ASME 105 (1996) 99–105.
[29] D. Hayhurst, Creep-rupture under multi-axial states of stress, J. Mech. Phys. Solids 20 (1972) 381–390.
[30] S. Marques, G. Creus, Computational Viscoelasticity, Springer, 2012.
[31] S. Park, Y. Kim, Fitting Prony-series viscoelastic models with power-law presmoothing, J. Mater. Civ. Eng. 13 (2001) 26–32.
[32] M. Kaliske, H. Rothert, Formulation and implementation of three-dimensional viscoelasticity at small and finite strains, Comput. Mech. 19 (1958) 228–239.
[33] M. Sedef, E. Samur, C. Basdogan, Real-time finite-element simulation of linear viscoelastic tissue behavior based on experimental data, IEEE Comput. Graph. Appl. (2006) 28–38.
[34] H. Brinson, L. Brinson, Polymer Engineering Science and Viscoelasticity, Springer, 2008.
[35] D. Gutierrez-Lemini, Engineering Viscoelasticity, Springer, 2014.
[36] J.-M. Schwartz, M. Denninger, D. Rancourt, C. Moisan, D. Laurendeau, Modelling liver tissue properties using a non-linear visco-elastic model for surgery simulation, Med. Image Anal. 9 (2005) 103–112.
[37] O. Sigmund, On the usefulness of non-gradient approaches in topology optimization, Struct. Multidiscip. Optim. 43 (2011) 589–596.
[38] P. Michaleris, Tangent operators and design sensitivity formulations for transient non-linear coupled problems with applications to elastoplasticity, Comput. Methods Appl. Mech. Engrg. 89 (1994) 309–336.
[39] Q. Wang, P. Moin, G. Iaccarino, Minimal repetition dynamic checkpointing algorithm for unsteady adjoint calculation, SIAM J. Sci. Comput. 31 (4) (2009) 2549–2567.

[40] A. Walther, A. Griewank, Advantages of binomial checkpointing for memory-reduced adjoint calculations, in: Numerical Mathematics and Advanced Applications, 2008, pp. 834–843.
[41] J.R.R.A. Martins, J.J. Alonso, The complex-step derivative approximation, ACM Trans. Math. Softw. 29 (2003) 245–262.
[42] K. Svanberg, The method of moving asymptotes—a new method for structural optimization, Int. J. Numer. Methods Optim. 24 (1987) 359–373.
[43] P. Grossman, T. Nakai, Deflection of wood under intermittent loading: part 2: cycles of two days and of 14 min, Wood Sci. Technol. 21 (1987) 349–360.
[44] T. Nakai, P. Grossman, Deflection of wood under intermittent loading, Wood Sci. Technol. 17 (1983) 55–67.
[45] F.J. Wortmann, K.V. Sculz, Stress relaxation and time/temperature superposition of polypropylene fibres, Polymer 36 (2) (1995) 315–321.
[46] M. Razavi-Nouri, Creep and stress relaxation behavior of polypropylene, metallocene-prepared polyethylene and their blends, Iran. J. Chem. Eng. 9 (2012) 60–69.
[47] E. Andreassen, Stress relaxation of polypropylene fibres with various morphologies, Polymer 40 (1999) 3909–3918.
[48] A.E. Akinay, Time–temperature correspondence prediction of stress relaxation of polymeric materials from a minimum of data, Polymer 43 (2002) 3593–3600.
[49] M. Deng, J. Zhou, Effects of temperature and strain level on stress relaxation behaviors of polypropylene sutures, J. Mater. Sci., Mater. Med. 17 (2006) 365–369.
[50] Y. Liu, A direct method for obtaining discrete relaxation spectra from creep data, Rheol. Acta 40 (2001) 256–260.
[51] R. Koeller, A theory relating creep and relaxation for linear materials with memory, J. Appl. Mech. 77 (2010) 1–9.
[52] C.G. Ek, B. Hagstrom, J. Kubat, M. Rigdahl, Prediction of the creep behaviour of polyethylene and molybdenum from stress relaxation experiments, Rheol. Acta 25 (1986) 534–541.
[53] I. Ward, J. Sweeney, Mechanical Properties of Solid Polymers, Wiley & Sons Ltd., 2012.
[54] C. Lawson, R. Hanson, Solving Least Squares Problems, Prentice Hall, 1974.